









The 3D Kinematics of Gas in the Small Magellanic Cloud

Claire E. Murray^{1,6} , J. E. G. Peek^{1,2} , Enrico M. Di Teodoro³ , N. M. McClure-Griffiths³ , John M. Dickey⁴ , and Helga Dénes⁵ 

¹Department of Physics & Astronomy, Johns Hopkins University, 3400 N. Charles Street, Baltimore, MD 21218, USA; clairemurray56@gmail.com

²Space Telescope Science Institute, 3700 San Martin Drive, Baltimore, MD 21218, USA

³Research School of Astronomy and Astrophysics—The Australian National University, Canberra, ACT, 2611, Australia

⁴School of Natural Sciences, Private Bag 37, University of Tasmania, Hobart, TAS, 7001, Australia

⁵ASTRON, Netherlands Institute for Radio Astronomy, Oude Hoogeveensedijk 4, 7991 PD, Dwingeloo, The Netherlands

Received 2019 September 4; revised 2019 October 15; accepted 2019 October 23; published 2019 December 26

Abstract

We investigate the kinematics of neutral gas in the Small Magellanic Cloud (SMC) and test the hypothesis that it is rotating in a disk. To trace the 3D motions of the neutral gas distribution, we identify a sample of young, massive stars embedded within it. These are stars with radial velocity measurements from spectroscopic surveys and proper motion measurements from *Gaia*, whose radial velocities match with dominant HI components. We compare the observed radial and tangential velocities of these stars with predictions from the state-of-the-art rotating disk model based on high-resolution 21 cm observations of the SMC from the Australian Square Kilometer Array Pathfinder telescope. We find that the observed kinematics of gas-tracing stars are inconsistent with disk rotation. We conclude that the kinematics of gas in the SMC are more complex than can be inferred from the integrated radial velocity field. As a result of violent tidal interactions with the Large Magellanic Cloud, nonrotational motions are prevalent throughout the SMC, and it is likely composed of distinct substructures overlapping along the line of sight.

Unified Astronomy Thesaurus concepts: [Galaxy kinematics \(602\)](#); [Interstellar medium \(847\)](#); [Radio astronomy \(1338\)](#); [Neutral hydrogen clouds \(1099\)](#); [Magellanic irregular galaxies \(1877\)](#); [Magellanic Clouds \(990\)](#)

Supporting material: extended figure, machine-readable table

1. Introduction

The Small Magellanic Cloud (SMC) is a gas-rich, low-metallicity ($Z \sim 0.2 Z_{\odot}$; Russell & Dopita 1992) dwarf irregular satellite of the Milky Way (MW). At a distance of ~ 62 kpc (e.g., Scowcroft et al. 2016), the SMC provides an ideal laboratory for studying the structure and kinematics of dwarf galaxies at high sensitivity and resolution.

As a result of its proximity to the MW and the nearby Large Magellanic Cloud (LMC), the SMC has been strongly influenced by ongoing dynamical interactions. The SMC and LMC likely experienced a direct collision ~ 150 Myr ago (e.g., Zivick et al. 2018) and their interactions have produced the broader, gaseous Magellanic System, including the Bridge (Hindman et al. 1963), Stream (Mathewson et al. 1974), and Leading Arm (Putman et al. 1998). In fact, low metallicities observed in the Stream and Leading Arm suggest that these structures originated, in part, from the SMC (Fox et al. 2013; D’Onghia & Fox 2016), and this premise is consistent with most models of the Magellanic System (Gardiner & Noguchi 1996; Connors et al. 2006; Besla et al. 2012; Diaz & Bekki 2012).

The complex dynamical history of the SMC has made it challenging to understand its present-day structure and kinematics. The neutral hydrogen (HI) in the system is highly disturbed (e.g., Stanimirović et al. 1999), featuring multi-peaked velocity profiles indicative of supergiant shells (Hindman 1967), two separate velocity subsystems (e.g., Mathewson et al. 1988), and/or hundreds of expanding shells (Staveley-Smith et al. 1997). However, despite this elaborate structure, the integrated velocity field of the SMC exhibits a strong gradient suggestive of

a nicely rotating disk (Kerr et al. 1954; Hindman et al. 1963; Stanimirović et al. 2004; Di Teodoro et al. 2019).

To complicate the picture further, observations of distinct stellar populations provide additional interpretations for the structure of the SMC. The oldest stars are spherically distributed within a radius of 7–12 kpc (Subramanian & Subramanian 2012), with little evidence for rotation from radial velocities or proper motions (PMs; Harris & Zaritsky 2006; Kallivayalil et al. 2013; Gaia Collaboration et al. 2018; Niederhofer et al. 2018; Zivick et al. 2018). Red clump stars and Cepheid variables are highly elongated along the line of sight (LOS; ~ 20 kpc depth; Mathewson et al. 1988; Nidever et al. 2013; Jacyszyn-Dobrzniecka et al. 2016; Scowcroft et al. 2016; Ripepi et al. 2017). Furthermore, although younger stellar populations and red giant branch (RGB) stars display a velocity gradient, it appears perpendicular to the gradient seen in HI (Evans & Howarth 2008; Dobbie et al. 2014). Similarly, the distance gradient observed in Cepheids from the northeast to southwest is $\sim 90^{\circ}$ from the minor axis, as implied by a rotating gas disk (Scowcroft et al. 2016).

Ultimately, although the observed distribution and kinematics of distinct mass tracers in the SMC have resulted in a diversity of interpretations for its structure, the rotating disk model derived from the HI velocity field remains a fundamental benchmark for our theoretical understanding of the SMC and the broader Magellanic System. Basic properties including its center of mass, halo composition, and total dynamical mass—fundamental for numerical models—are derived from the rotation curve analysis (Stanimirović et al. 2004; Di Teodoro et al. 2019). Furthermore, the SMC LOS depth inferred from the HI velocity field is routinely invoked to estimate the surface densities of molecular gas and star

⁶ NSF Astronomy & Astrophysics Postdoctoral Fellow.

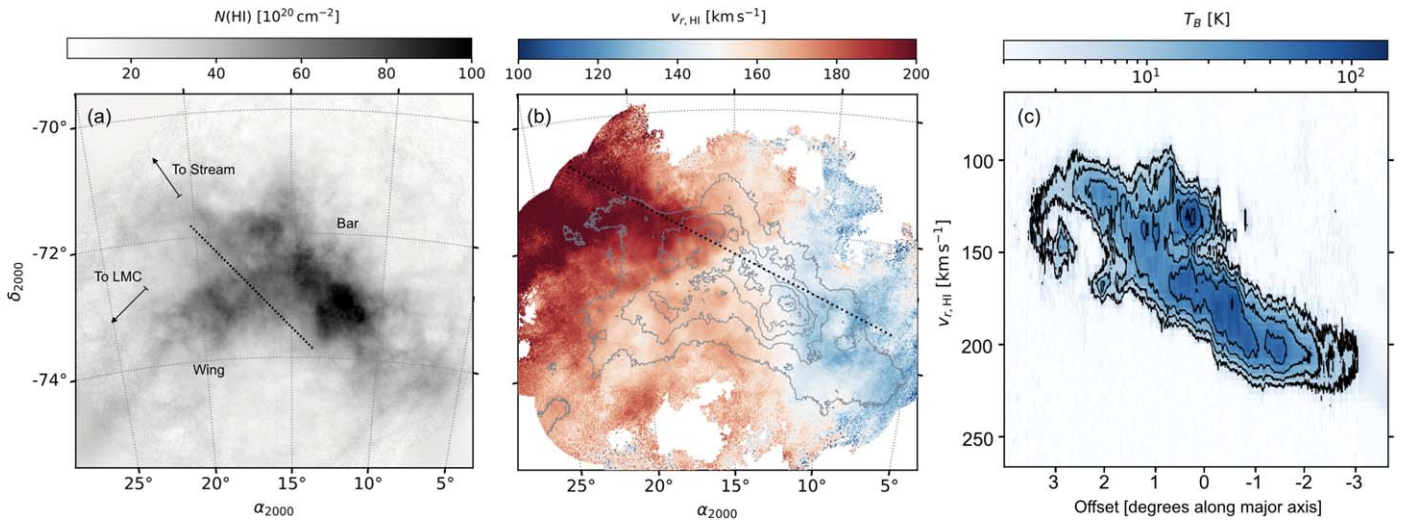


Figure 1. (a) H I column density map of the SMC from the ASKAP+Parkes data cube. The dotted line delineates the main “Bar” from the “Wing” of the SMC, and arrows indicate the directions of the Magellanic Stream and the LMC (following McClure-Griffiths et al. 2018). (b) The first moment map, masked as described in Section 2.1. The contours (gray) display $N(\text{HI})$ at levels of [15, 35, 55, 75, 95, 115] $\times 10^{20} \text{ cm}^{-2}$. The dotted line (black) indicates the major axis inferred from kinematic modeling of the ASKAP+Parkes data cube (center: $\alpha_{2000} = 15^{\circ}237$, $\delta_{2000} = -72^{\circ}273$, position angle: 66° ; Di Teodoro et al. 2019). (c) The position–velocity slice through the center of the SMC and along the major axis (shown in panel (b)). Contours are drawn at $T_B = 3 \times 2'' \text{ K}$.

formation in the system. For example, although the star formation efficiency of molecular gas is the same in the SMC as within large spiral galaxies, the ratio of molecular to atomic gas is an order of magnitude lower (Jameson et al. 2016) implying that the SMC is “strikingly bad” at converting its atomic gas reservoir into stars (Bolatto et al. 2011). Although the interaction history between the SMC and the LMC and MW may have affected this capability by removing gas from the system, this result is invoked to explain similarly suppressed star formation rate efficiencies of H I-dominated galaxies at $z \sim 1\text{--}3$ (e.g., Wolfe & Chen 2006; Rafelski et al. 2016). Although the result can be alleviated by varying uncertain disk parameters, such as its inclination, a preferable model remains elusive.

Ultimately, reconciling the disparate kinematics of gas and stars in the SMC and testing the rotating disk hypothesis requires constraints for the 3D kinematics of gas in the system. Previous models were based on the radial velocity alone, as this is the only observable velocity component for the gas. In this paper, we constrain the 3D motions of gas within the SMC using the measured 3D motions of embedded young stars (O and B type). In Section 2, we present the pertinent observations and models; in Section 3, we discuss the methods used to analyze the observations; in Section 4, we present the results of comparing the observed kinematics with predictions from the rotating disk model; and in Section 5, we discuss the implications for the SMC system.

2. Data

Although the radial motions of the SMC gas distribution are well measured by radio observations of neutral gas tracers (e.g., H I), the transverse motions are unconstrained. We assume that massive stars whose radial velocities match with the gaseous components formed recently enough ($\sim 1\text{--}10 \text{ s Myr}$ lifetimes) to trace the 3D motions of the same gas that they are embedded within, and we use the measured transverse velocities of these stars to trace the transverse motions of the underlying gas. To avoid confusion with stars that have migrated away from their original gas clouds (Oey et al. 2018), we make a very

conservative selection to generate a small sample of 143 stars whose velocities match closely with clearly defined peaks in the 21 cm spectra in their directions. This velocity matching step rejects some 88% of the original sample of stars, but the remaining stars are the most likely to show the same disk rotation that the gas shows.

2.1. Neutral Gas

As the SMC is rich in neutral atomic gas (e.g., Leroy et al. 2007), we use H I to trace the gas distribution. New observations of the SMC at 21 cm were recently obtained by the Australian Square Kilometer Array Pathfinder (ASKAP; DeBoer et al. 2009) during Commissioning and Early Science observations in 2017 November. These data were combined with single-dish observations of the SMC from the Parkes Telescope as part of the HI4PI survey (HI4PI Collaboration et al. 2016). For details concerning the observations and data reduction for the ASKAP+Parkes cube, we refer the reader to McClure-Griffiths et al. (2018). The final data cube we use has an rms noise in 21 cm brightness temperature (T_B) of $\sigma_{T_B} = 0.7 \text{ K}$, a pixel size of $7''$ ($35'' \times 27''$ in angular resolution), and velocity channel width of 3.9 km s^{-1} (McClure-Griffiths et al. 2018; Di Teodoro et al. 2019). For comparison with stellar velocities, we convert the H I velocities from the local standard of rest to the heliocentric reference frame. Hereafter, all quoted velocities will be in the heliocentric reference frame.

In Figure 1, we display a map of the H I column density ($N(\text{HI})$) of the SMC from the ASKAP+Parkes data cube (panel (a)), the first moment map (panel (b)), and a position–velocity slice along the major axis inferred from kinematic modeling of the H I data cube by Di Teodoro et al. (2019); panel (c), see Section 2.4). The moment map is masked as in Di Teodoro et al. (2019), wherein a flood-fill algorithm applied to a smoothed version of the data cube (smoothed with a Gaussian kernel of FWHM $70''$) identified pixels with emission brighter than $\sim 10\sigma_{\text{HI}}$, out to pixels with $\sim 4\sigma_{\text{HI}}$ (where σ_{HI} is the rms of the smoothed data).

2.2. Stars

We select a subsample of SMC stars with measured radial velocities from the spectroscopic survey of the SMC by the 2-degree-field instrument at the Anglo-Australian Telescope (2045 stars; Evans & Howarth 2008) and from the Runaways and Isolated O-Type Star Spectroscopic Survey of the SMC (RIOTS4), a uniformly selected survey of young field stars in the SMC using the Inamori-Magellan Areal Camera and Spectrograph (IMACS) and Magellan Inamori Kyocera Echelle (MIKE) on the Magellan telescopes (374 stars; Lamb et al. 2016). Of this sample, 1484 stars are of spectral type O or B and have significant radial velocity (v_r) measurements (defined as $v_r/\sigma_{v_r} > 5$, where σ_{v_r} is the uncertainty on the radial velocity measurement).

To determine the transverse velocities of the selected stars, we cross-match them with SMC stars from the second data release (DR2) of the *Gaia* mission (Gaia Collaboration et al. 2018). The targets observed by Evans & Howarth (2008) and Lamb et al. (2016) were selected from the original catalog by Massey (2002), who reported a positional uncertainty of $1''$ per target. We begin with a conservative search radius of 3σ and find unique 1451 *Gaia* sources within $3''$ of the selected stars. All matched targets have significant PM (μ) detections in R.A. (α) and decl. (δ) ($\mu_\alpha/\delta_{\mu_\alpha} > 5$ and $\mu_\delta/\delta_{\mu_\delta} > 5$ where δ_{μ_α} and δ_{μ_δ} are the uncertainties in R.A. and decl. proper motions, respectively). The matched stars represent the youngest, brightest end of the population observed by *Gaia*; for example, the median *Gaia* G magnitude for the matched sample is $G = 15.3$, compared with the median magnitude for the full SMC sample of $G = 19$. We further refine the sample by comparing the observed flux densities and remove 249 objects with discrepant $G - B$ colors (defined as being further from the mean $G - B$ color of 0.16 by more than $\pm 1\sigma = 0.47$). The final sample contains 1202 sources.

2.3. Systemic Proper Motion

To estimate the PMs due to internal motions of the SMC, we subtract the systemic motion of the galaxy from the measured *Gaia* PMs. For consistent comparison with the latest dynamical modeling of the system (see Section 2.4), we adopt the measured center of mass (COM) PM derived from *Hubble Space Telescope* photometry by Kallivayalil et al. (2013), who estimated $\mu_{W,0} = -0.772 \pm 0.063$ mas yr $^{-1}$ and $\mu_{N,0} = -1.117 \pm 0.061$ mas yr $^{-1}$. We note that many studies have estimated the COM PM of the SMC (e.g., Piatek et al. 2008; Kallivayalil et al. 2013; van der Marel & Sahlmann 2016; Niederhofer et al. 2018; Zivick et al. 2018), and all estimates are largely consistent within uncertainties.

2.4. Dynamical Model

For comparison with the observed kinematics, we use the results of a recent dynamical model in the SMC by (Di Teodoro et al. 2019, hereafter DT19) based on the ASKAP+Parkes HI data cube. DT19 modeled the SMC as a disk undergoing circular rotation. Using a Markov Chain Monte Carlo (MCMC) approach, they fitted the observed velocity field (e.g., Figure 1(b)) to derive global properties of the system, including kinematic center, position and inclination angles, transverse and systemic velocities, and then applied a tilted-ring analysis to decompose the velocity field and extract the rotation velocity as a function of radius.

Using the DT19 results, we predict the velocities for stars within a rotating SMC based on their coordinates. To compute each velocity component, we follow van der Marel & Cioni (2001, hereafter vdM2001) and van der Marel et al. (2002, hereafter vdM2002). We assume the same global SMC parameters as derived in the DT19 model, including: the SMC COM ($\alpha_{0,2000} = 15.237 \pm 0^\circ.380$, $\delta_{0,2000} = -72.273 \pm 0^\circ.290$), distance ($D_0 = 63 \pm 5$ kpc), COM PM ($\mu_{W,0} = -0.772 \pm 0.063$, $\mu_{N,0} = -1.117 \pm 0.061$ mas yr $^{-1}$; Kallivayalil et al. 2013), systemic LOS velocity (Heliocentric, $v_{r,\text{sys}} = 157 \pm 2$ km s $^{-1}$), inclination ($i = 55^\circ \pm 9^\circ$), position angle of the line of nodes (PA = $66^\circ \pm 8^\circ$; measured counterclockwise from north) and precession and nutation rate ($\partial i/\partial t = -281^\circ \pm 100^\circ$ Gyr $^{-1}$). From the assumed COM PM, we also compute the transverse velocity of the COM and its angle on the sky.

Given these global parameters, for each star, we compute its angular coordinates on the sky (Equations (1)–(3), vdM2001), its radius in the galaxy frame (Equation (9), vdM2002) and its ensuing predicted rotation velocity from the DT19 model. We then follow vdM2002 to compute the individual velocity contributions from the SMC COM (Equation (13), vdM2002), its precession and nutation (Equation (16), vdM2002) and internal motions (Equation (21), vdM2002). The sum of these components comprise the predicted velocities in the frame of the SMC. Finally, we extract the predicted radial velocity ($v_{r,\text{Model}}$) and the PMs to the west and north ($\mu_{W,\text{Model}}$ and $\mu_{N,\text{Model}}$; Equation (9), vdM2002) for comparison with the observed sample. As an estimate of the uncertainties in these predictions, we propagate the quoted uncertainties in the nine global SMC parameters from DT19 through the analysis.

3. Analysis

3.1. Line-of-sight Complexity

Although the radial velocity structure of HI in the SMC is complex, it has been shown that a significant fraction of OB stars have coincident radial velocities with HI structures along the same LOS and are, therefore, embedded within the HI distribution (Lamb et al. 2016). Although the majority of young stars are associated with some HI emission, our goal is to construct a pure sample of targets that are most likely to trace the motions of dominant HI components.

We begin by identifying significant HI components along each LOS in the ASKAP+Parkes data cube via the derivative of $T_B(v_r)$. First, we resample each $T_B(v_r)$ spectrum to 0.5 km s $^{-1}$ resolution and smooth with a Gaussian kernel eight channels in width to suppress the influence of noise on selecting spurious peaks. We then compute the first numerical derivative of each spectrum and identify components as local maxima with significant emission ($T_B > 5$ K). Figure 2 displays the total number of significant HI components along each LOS. Although the outskirts of the SMC typically feature a single strong HI component, within the main body of the SMC the radial velocity structure of the gas is more complex and there are at least two HI components. This is evident in Figure 1(c); in addition to the “main disk” of the SMC along the major axis inferred by rotation models, there are several significant velocity components evident in the position–velocity diagram.

3.2. Matching Radial Velocities

To identify which stars are moving with the identified HI components, we compare the observed stellar radial velocities

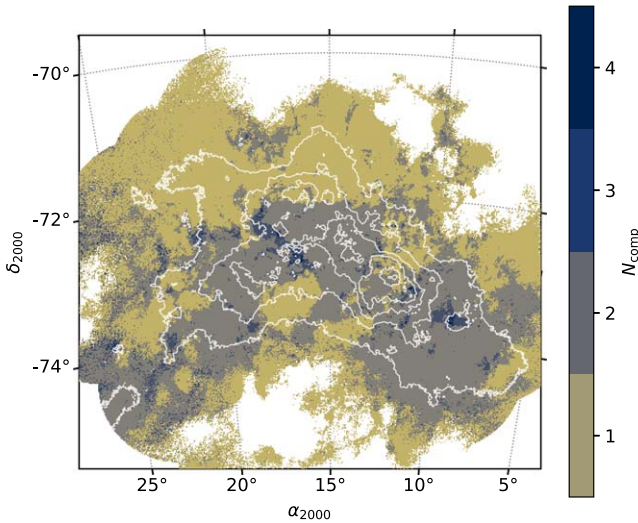


Figure 2. Map of the total number of significant H I components (N_{comp}), masked as described in Section 2.1. White contours denote $N(\text{H I})$ at levels of $[15, 35, 55, 75, 95, 115] \times 10^{20} \text{ cm}^{-2}$.

($v_{r,\text{star}}$) with the radial velocities of the H I components ($v_{r,\text{H I}}$). To select the most likely sources to trace the dominant H I along each LOS, we design a method for matching stars with H I components which accounts for the uncertainties in $v_{r,\text{star}}$, which can be large ($\sigma_{v_{r,\text{star}}} \sim 5\text{--}30 \text{ km s}^{-1}$; Evans & Howarth 2008; Lamb et al. 2016).

For each star, we select $N = 1000$ velocities distributed normally with mean $v_{r,\text{star}}$ and $\sigma = \sigma_{v_{r,\text{star}}}$. For each H I component, we construct similar normally distributed velocity distributions with mean $v_{r,\text{H I}}$ and an assumed $\sigma = \sigma_{\text{H I}} \text{ km s}^{-1}$. We then use a two-sample Anderson–Darling test (A–D; Anderson & Darling 1954) to test for the null hypothesis that the stellar and H I velocity distributions are drawn from the same parent population. A match is achieved if the null hypothesis cannot be rejected with high confidence ($>99\%$), and if the brightness temperature of the H I peak is above a certain fraction of the max T_{B} along the LOS (r_{peak} , where $r_{\text{peak}} = T_{\text{B,peak}}/\max(T_{\text{B}}(v_r))$), to ensure that matches are with dominant H I peaks.

To select the optimal values for the matching parameters ($\sigma_{\text{H I}}$ and r_{peak}), we repeat the match process for a range of values ($1 < \sigma_{\text{H I}} < 10 \text{ km s}^{-1}$ and $0 < r_{\text{peak}} < 1$) and select the values that maximize the number of matches while minimizing the contamination fraction. To quantify the contamination of the sample due to random interlopers with coincidental radial velocities to the H I peaks, we repeat the matching process using simulated samples of 1202 stars with random velocities and uncertainties drawn from the observed distributions over 1000 trials. The estimated number of spurious matches is computed as the median over all trials. We find that the choice of $\sigma_{\text{H I}}$ and r_{peak} does not have a significant effect on the results, and the contamination fraction is $\sim 25\%$ for all tested values. We will discuss the effect of this contamination fraction in Section 4. We select $\sigma_{\text{H I}} = 5 \text{ km s}^{-1}$ and $r_{\text{peak}} = 0.3$.

We note that this approach produces statistically indistinguishable results from other methods of matching $v_{r,\text{star}}$ and $v_{\text{H I}}$, including: (1) by-eye matching, (2) applying a range of absolute cuts to $\Delta v_r = |v_{r,\text{star}} - v_{r,\text{H I}}|$, and (3) computing the area of overlap between the $v_{r,\text{star}}$ and $v_{r,\text{H I}}$ distributions and applying a sigma cut.

To determine the final sample, we repeat the matching process with the selected match criteria over an additional 1000 trials and select all stars that have successful matches in more than 95% of the trials. The result is a sample of 143 stars. The matched sources are shown in Figure 3. In the Appendix, we include similar figures for all LOS (Figure 6).

Although the final sample represents only $\sim 12\%$ of the initial sample of stars with both radial and transverse velocity constraints (1202 sources), this does not mean that the remaining 88% of the sample are not associated with H I gas. In fact, we observe that the majority of the initial sample of 1202 stars ($\sim 80\%$) is associated with significant H I emission, which is defined as there being significant H I emission at the radial velocity of the star ($T_{\text{B}}(v_{r,\text{star}}) > 5 \text{ K}$). This indicates that most stars are embedded somewhere within the neutral gas distribution, if not associated with the strongest peaks. The final sample of 143 matched stars represents our highest confidence for tracing the H I kinematics with minimal contamination. We further observe that although relaxing the matching criteria (e.g., including wider uncertainty ranges, selecting different brightness temperature cuts to define H I components, etc.) changes the number and selection of stars that are included in the matched sample, it does not significantly affect the statistics of the sample (e.g., estimated contamination fraction) or the ensuing conclusions.

4. Results

In Figure 4(a), we display the residual PMs (i.e., with the COM PM from Kallivayalil et al. 2013 subtracted) for the 143 stars whose radial velocities match with significant H I peaks. The stars exhibit a radial velocity gradient in agreement with the H I radial velocity field (Figure 1(b)). However, the observed residual PMs do not exhibit a clear signature of rotation. For comparison, in Figure 4(b), we display the radial velocities and residual PMs predicted by the DT19 rotation model. As expected, the modeled residual PMs exhibit a clear signature of rotation.

Comparing the panels of Figure 4, although the observed and modeled kinematics are not consistent throughout the SMC, the level of agreement may depend on location within the system. For example, a subset of stars have large observed tangential velocities ($\sim 100 \text{ km s}^{-1}$). These large velocities are likely dominated by dynamical effects (Oey et al. 2018). Stars in the the Wing region (southeast, see Figure 1(a)) are moving toward the LMC via the Magellanic Bridge as a result of their recent interaction history (Zivick et al. 2019). Furthermore, this net PM of the Wing relative to the Bar indicates that these two regions may be kinematically distinct (Oey et al. 2018). Although stars and gas throughout the SMC are affected at some level by the same dynamical interactions, in subsequent analysis, we will distinguish stars in the Wing and Bar to account for the possibility that stars in different regions are tracing distinct populations.

In Figure 5, we compare the observed and predicted radial (LOS) velocity (a), and the residual PMs to the west and north ((b) and (c), respectively) for the 143 matched stars. Stars located in Wing and Bar are distinguished from each other for clarity (see Figure 1(a) for definitions).

Figures 4 and 5 indicate that the observed kinematics are largely inconsistent with the predictions from the rotating disk model. To quantify the agreement, we use the K-sample A–D statistic. First, we bootstrap the sample with replacement over

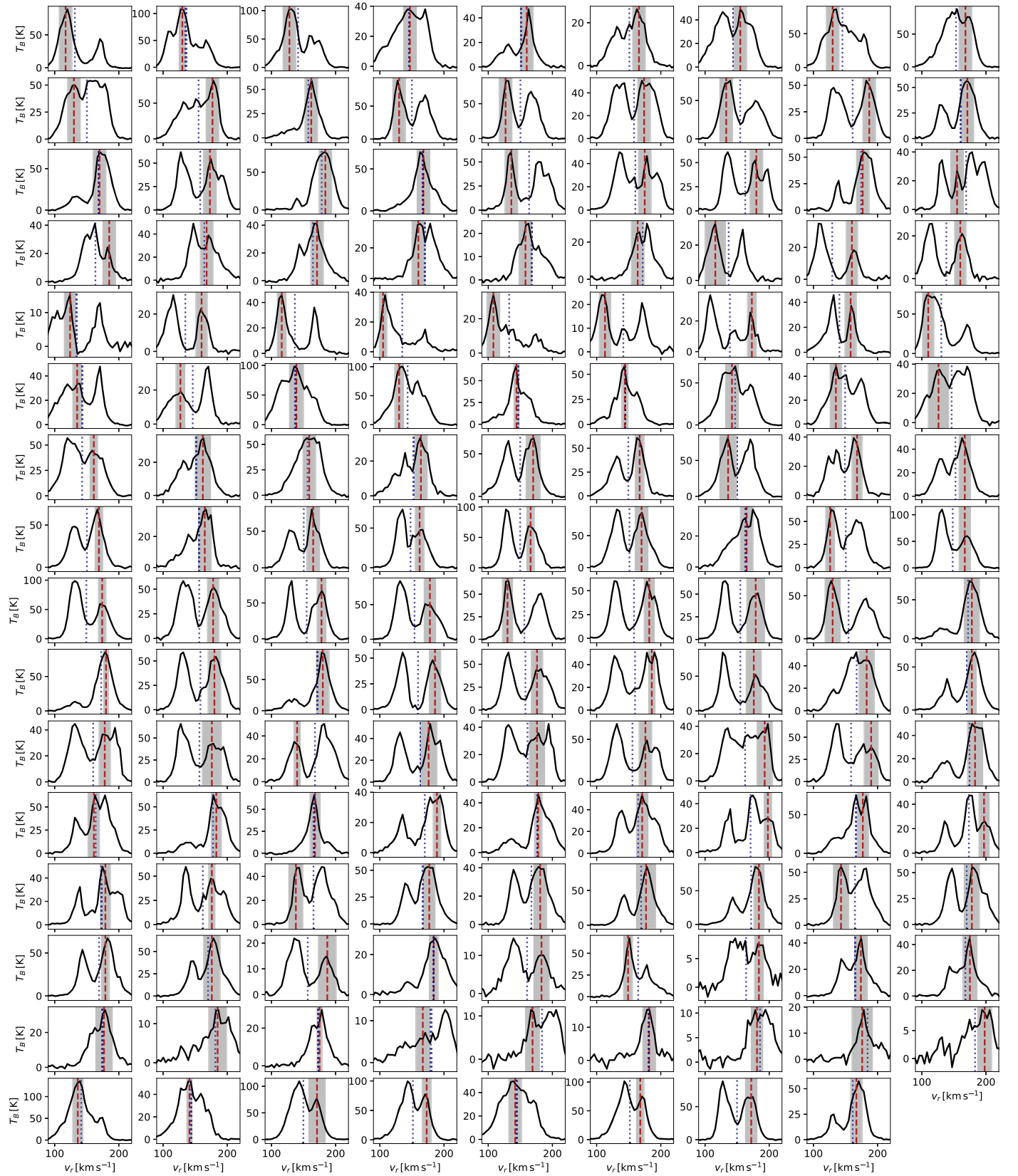


Figure 3. Results of matching observed radial velocities of young, massive stars (red dashed) with the radial velocities of distinct H I peaks along the same LOS (black). For each of the 1202 stars with radial and transverse velocity measurements, over 1000 trials, we sample random velocities within $\pm 1\sigma_v$ (gray) and find the 143 LOS that “match” (see Section 3.2). The $\pm 1\sigma$ uncertainties on the $v_{r,\text{star}}$ are illustrated (gray shading), and the first moment (Figure 1(b)) is included (blue dotted line).

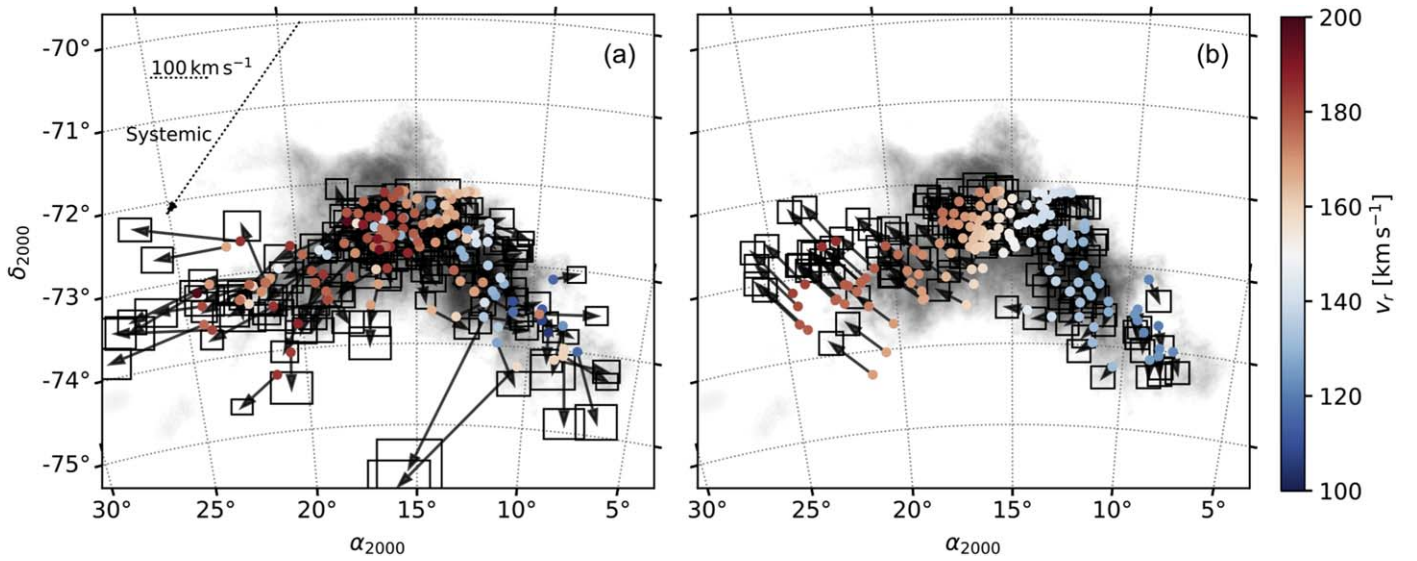


Figure 4. (a) Radial velocities (color) and residual PMs (vectors) for the sample of 143 stars with significantly detected radial and transverse motions from spectroscopy (Evans & Howarth 2008; Lamb et al. 2016) and *Gaia* (Gaia Collaboration et al. 2018), whose radial velocities match significant H I components along the LOS (see Figure 3). All vectors are constructed to illustrate PMs over the next 7.2 Myr (arbitrarily, as in van der Marel & Sahlmann 2016). The systemic PM of the SMC (Kallivayalil et al. 2013) is included at top left (dotted), as is a scale bar to illustrate 100 km s^{-1} (dashed). (b) Same, for the predicted radial velocities and residual PMs (black vectors) from the SMC rotation model by DT19.

1000 trials, and within each trial, we use a simple Monte Carlo exercise to draw random values of each velocity component within $\pm 3\sigma$ to compute the A–D statistic. The final value is a median over all trials. We find that the null hypothesis that the observed and modeled velocity distributions are drawn from the same parent population is ruled out with $>99\%$ confidence for v_r , μ_W , and μ_N for the full sample. When treating the two regions of the SMC separately, the agreement does not improve significantly: the null hypothesis is ruled out in all cases with $>99\%$ confidence again, with the exception of the radial velocity of the Wing (98% confidence). To explicitly and conservatively account for the estimated 25% contamination from random interlopers, we repeat the above exercise and exclude the worst 25% in each trial (defined as those points with the largest absolute difference between observed and modeled velocities). We find consistent results as for the full sample (agreement ruled out with $>99\%$ confidence, despite some improvement in the Bar and Wing subsamples) except for the cases of μ_W for the full sample (98% confidence).

5. Discussion

Overall, the observed 3D kinematics of H I in the SMC traced by young massive stars are inconsistent with predictions from the rotating disk model. In the following, we discuss how to reconcile this result within the context of the SMC.

First, it is important to consider alternatives to the hypothesis that the SMC is well represented by a single rotating disk. As discussed by DT19, there are several caveats to the disk model, including the fact that the disk is not razor thin (as must be assumed to simplify the velocity component computation), the rotation is not necessarily perfectly circular, and the disk is not necessarily axisymmetric. In addition to these caveats, there is clear evidence that significant components of the system (e.g., the Wing) are dominated by radial motions due to the influence of the LMC (e.g., Zivick et al. 2019). The fact that the rotation model performs as well as it does at reproducing the radial velocity field of the gas suggests that the large scale motion is

dominated by rotation and the discrepant stellar kinematics observed here may reflect only local, noncircular motions. Although a subset of our sample likely does trace local motions (e.g., effects of stellar feedback on small scales), the majority were selected to trace the dominant H I components. As seen in Figure 5(a), the observed radial velocities of stars matched to H I peaks trace distinct, coherent components in radial velocity—one at $\sim 130 \text{ km s}^{-1}$ and one at $\sim 160 \text{ km s}^{-1}$ —which are found in both the Wing and the Bar. The intensity-weighted mean velocity along each LOS used to predict 3D gas motions can be insensitive to this multiplicity, especially if there are multiple components with similar intensities. To illustrate this effect, in Figure 3, we include the first moment for comparison with the H I peak velocities along each LOS. In addition, we note that although *Gaia* PMs in the SMC display a marginal signal of rotation (Gaia Collaboration et al. 2018, their Figure 16), it is inconsistent with the rotation inferred from the H I.

An alternative explanation for the discrepancy between the observed and model kinematics is that the SMC is not a single system but is rather composed of multiple structures along the LOS. As illustrated in Figures 2 and 5, the structure of the SMC is complex and exhibits multiple, significant H I components separated in radial velocity. This velocity structure has previously been attributed to separate subsystems within the SMC (e.g., the Mini Magellanic Cloud and the SMC Remnant; Mathewson et al. 1984), which may be separated in distance along the LOS by $>10 \text{ kpc}$ (Mathewson et al. 1986). Based on measurements of ultraviolet absorption lines toward stars in the SMC, the lower-velocity H I component appears to be sitting in front of the higher-velocity H I component along the LOS (Songaila et al. 1986; Wayte 1990; Danforth et al. 2002; Welty et al. 2012). This implies that the SMC is being ripped apart by its interactions with the LMC, which is in agreement with tidal models of the system (Murai & Fujimoto 1980), resulting in disparate remnant structures.

If the SMC is composed of separate subsystems at different distances, it is possible that the apparent rotation seen in the radial velocity field of the gas is dominated by rotation within one

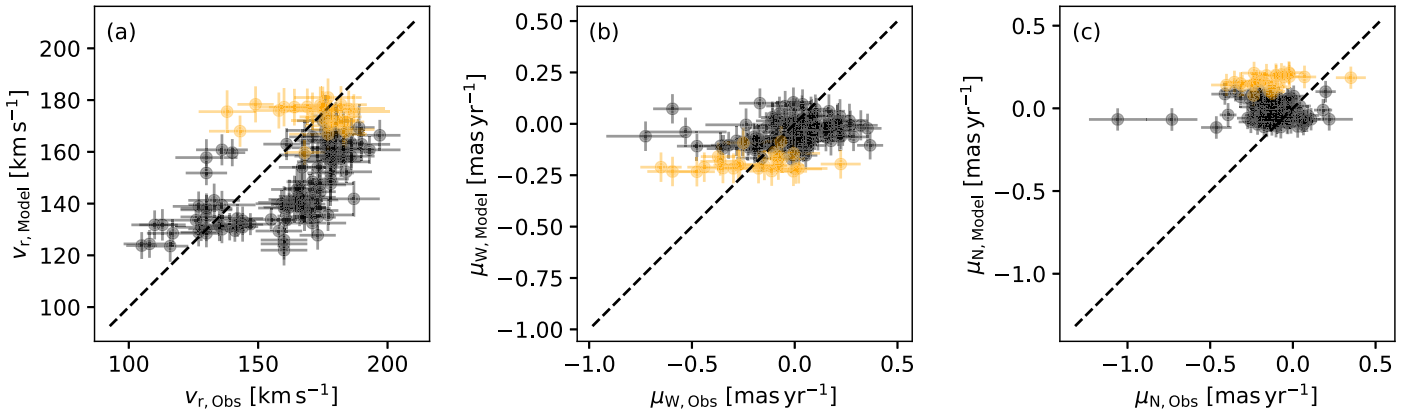


Figure 5. Comparison between radial velocity (v_r) and PMs to the west and north (μ_W and μ_N) observed (“Obs”) and predicted by DT19 (“Model”) for the sample of 143 stars whose radial velocities match significant H I components. The error bars on $v_{r,Obs}$ are 1σ uncertainties (Evans & Howarth 2008; Lamb et al. 2016), and the error bars on $\mu_{W,obs}$ and $\mu_{N,obs}$ are 1σ uncertainties from the *Gaia* DR2 catalog (Gaia Collaboration et al. 2018). The error bars for the “Model” parameters are estimated by propagating the uncertainties in the global SMC parameters through the velocity calculations (see Section 2.4). We divide the sample by location in the SMC (see Figure 1(a) for definitions): the Bar (black) and Wing (orange).

component over the other. However, exactly how we can reconcile potential rotation in this component alone with the nonrotating kinematics of the rest of the SMC is uncertain and is not incorporated into current theoretical models. In addition, it has been shown that models with purely radial motions can reproduce observed velocity fields just as well as disk models with purely rotational motion (e.g., Sylos Labini et al. 2019). Furthermore, the derived global properties of the system, including its dynamical center and mass—crucial input parameters to numerical models of the broader Magellanic System (Besla et al. 2012)—are based on fits to the global radial velocity field (e.g., including all velocities along each LOS; Figure 1). If only subsets of the SMC are actually rotating, these models (and the resulting parameters) would still need to be revisited.

6. Summary and Conclusions

In this paper, we present new constraints for the 3D kinematics of gas in the SMC. We trace the transverse motions of H I in the system for the first time using the observed proper motions of massive, young stars whose radial velocities match with significant H I components identified from new observations by the ASKAP telescope (McClure-Griffiths et al. 2018). We test the hypothesis that gas in the SMC is rotating in a disk by comparing the observed radial and transverse velocities of young stars with predictions from the latest model of the radial velocity field from DT19. Our main conclusions are the following:

1. The observed motions of gas-tracing stars are inconsistent with the predictions from the DT19 rotation model, even when the contamination from random interlopers is explicitly taken into account (Figures 4 and 5).
2. The 3D kinematics of the SMC are more complex than can be accurately inferred from the integrated radial velocity field alone.
3. Due to violent tidal and ram-pressure interactions with the LMC and the MW halo, it is likely that the SMC is composed of overlapping substructures, whose properties should be considered in future models of the system for extracting basic parameters, such as the COM, dynamical mass, and depth along the LOS.

Overall, this study represents one step in the process of unraveling the structure and kinematics of the SMC. In the near

future, with the third data release from *Gaia*, we will have access to radial velocity measurements toward a new sample of stars throughout the SMC with which we will further dissect the kinematics of individual gaseous components. In addition, with resolved stellar photometry, we will constrain the distances to individual dusty components and complete the full 6D phase space of the system (3D positions and 3D velocities). As the Magellanic Clouds are the only systems for which we can achieve this level of resolution, this will not only inform our understanding of these systems but also our understanding of dwarf galaxy interactions throughout cosmic time.

We would like to thank the anonymous referee for thoughtful comments that have improved this manuscript. C.E.M. is supported by an NSF Astronomy and Astrophysics Postdoctoral Fellowship under award AST-1801471. N.Mc.-G. acknowledges funding from the Australian Research Council via grant FT150100024. This work took part under the program Milky Way-*Gaia* of the PSI2 project funded by the IDEX Paris-Saclay, ANR-11-IDEX-0003-02. This research has made use of NASA’s Astrophysics Data System. The Australian SKA Pathfinder is part of the Australia Telescope National Facility which is managed by CSIRO. Operation of ASKAP is funded by the Australian Government with support from the National Collaborative Research Infrastructure Strategy. ASKAP uses the resources of the Pawsey Supercomputing Centre. Establishment of ASKAP, the Murchison Radio-astronomy Observatory and the Pawsey Supercomputing Centre are initiatives of the Australian Government, with support from the Government of Western Australia and the Science and Industry Endowment Fund. We acknowledge the Wajarri Yamatji people as the traditional owners of the Observatory site.

Software: Astropy (Astropy Collaboration et al. 2013), NumPy (Van Der Walt et al. 2011), matplotlib (Hunter 2007), glue (Beaumont et al. 2015).

Appendix Matching Radial Velocities

In this appendix, we provide supplemental figures and tables for illustrating the match process between the observed radial velocities of young, massive stars (Evans & Howarth 2008; Lamb et al. 2016) and the observed radial velocities of significant H I peaks along the same LOS. In Figure 6, we display plots for

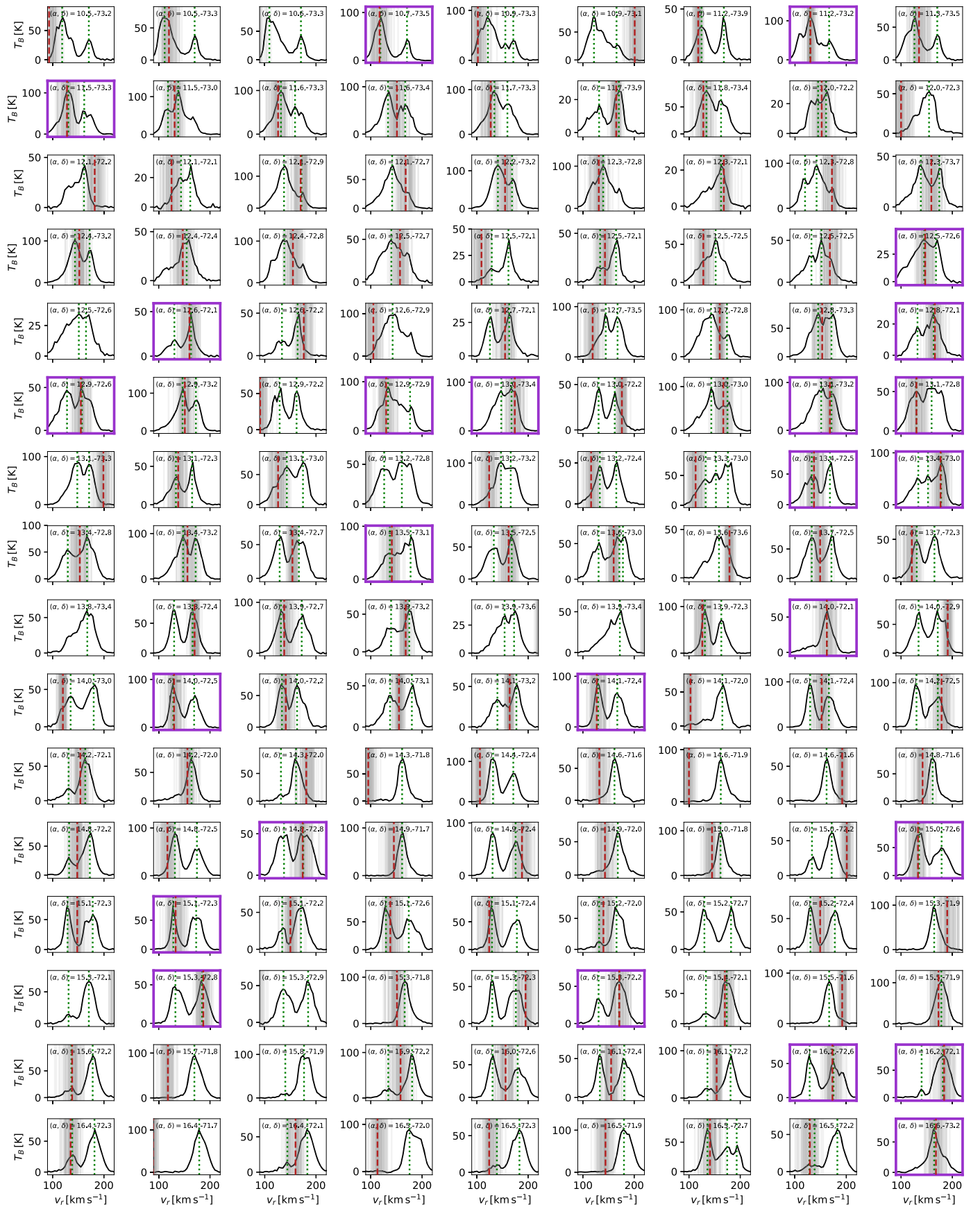


Figure 6. Each panel compares the 21 cm $T_B(v_r)$ spectrum and identified H I components ($v_{r,\text{H I}}$; dotted green lines) with the observed stellar radial velocity ($v_{r,\text{star}}$; red dashed line). The uncertainties in $v_{r,\text{star}}$ are illustrated by 50 random draws from a normal distribution with $\mu = v_{r,\text{star}}$ and $\sigma = \sigma_{v_{r,\text{star}}}$ (gray). The 143 matches (see the text) are highlighted by bold, purple plot frames (also see Figure 3). If $v_{r,\text{star}}$ is not visible within the panel, it falls outside the plotted velocity range. (An extended version of this figure is available.)

Table 1
Parameters for the 143 Stars Used in the Kinematic Comparison

R.A.	Decl.	$v_{r,\text{star}}$	$\delta v_{r,\text{star}}$	Type	References	μ_W	μ_N	$\delta\mu_W$	$\delta\mu_N$
(1)	(2)	(3)	(4)	(5)	(6)	(7)	(8)	(9)	(10)
7.798	-73.993	116.0	16.0	B1-3 (V)	2	-0.656	-1.550	0.127	0.107
8.410	-73.973	160.0	9.0	B1-3 (IV)	2	-0.772	-1.580	0.125	0.092
8.412	-74.064	160.0	9.0	B9 (Ib)	2	-0.501	-1.274	0.067	0.050
8.565	-73.694	124.0	9.0	B3-5 (III)	2	-0.834	-1.402	0.136	0.107
8.793	-74.122	160.0	9.0	B9 (II)	2	-0.450	-1.190	0.082	0.069
9.178	-73.137	116.0	7.0	B8 (II)	2	-0.628	-1.088	0.056	0.049
9.178	-73.794	105.0	6.0	B8 (II)	2	-0.782	-1.291	0.097	0.069
9.504	-73.652	108.0	10.0	B9 (Ib)	2	-0.593	-1.219	0.047	0.043
9.536	-73.516	113.0	9.0	B9 (II)	2	-0.712	-1.269	0.055	0.051
9.641	-73.579	173.0	7.0	B1-3 (II)	2	-0.418	-1.128	0.068	0.056







Note. (1), (2): R.A., decl. coordinates; (3), (4): observed radial velocity and uncertainty; (5) stellar type; (6) radial velocity reference: 1 = Lamb et al. (2016) and 2 = Evans & Howarth (2008); (7)–(10): PMs and uncertainties in the west; (7), (9) north; and (8), (10) directions from Gaia Collaboration et al. (2018).

(This table is available in its entirety in machine-readable form.)

each of 1202 stars with significant radial velocities with corresponding proper motion measurements from *Gaia* DR2 (Gaia Collaboration et al. 2018). We include the HI spectrum ($T_B(v_r)$) and the identified significant components along each LOS. The 143 matched LOS are identified by purple plot frames (and are also shown in Figure 3).

In Table 1, we include the coordinates, velocities, and PMs for the 143 HI-matched stars.

ORCID iDs

Claire E. Murray  <https://orcid.org/0000-0002-7743-8129>
 J. E. G. Peek  <https://orcid.org/0000-0003-4797-7030>
 Enrico M. Di Teodoro  <https://orcid.org/0000-0003-4019-0673>
 N. M. McClure-Griffiths  <https://orcid.org/0000-0003-2730-957X>
 John M. Dickey  <https://orcid.org/0000-0002-6300-7459>
 Helga Dénes  <https://orcid.org/0000-0002-9214-8613>

References

- Anderson, T. W., & Darling, D. A. 1954, *J. Am. Stat. Assoc.*, 49, 765
 Astropy Collaboration, Robitaille, T. P., Tollerud, E. J., et al. 2013, *A&A*, 558, A33
 Beaumont, C., Goodman, A., & Greenfield, P. 2015, in ASP Conf. Ser. 495, *Astronomical Data Analysis Software and Systems XXIV*, ed. A. R. Taylor & E. Rosolowsky (San Francisco, CA: ASP), 101
 Besla, G., Kallivayalil, N., Hernquist, L., et al. 2012, *MNRAS*, 421, 2109
 Bolatto, A. D., Leroy, A. K., Jameson, K., et al. 2011, *ApJ*, 741, 12
 Connors, T. W., Kawata, D., & Gibson, B. K. 2006, *MNRAS*, 371, 108
 Danforth, C. W., Howk, J. C., Fullerton, A. W., Blair, W. P., & Sembach, K. R. 2002, *ApJS*, 139, 81
 DeBoer, D. R., Gough, R. G., Bunton, J. D., et al. 2009, *IEEEP*, 97, 1507
 Di Teodoro, E. M., McClure-Griffiths, N. M., Jameson, K. E., et al. 2019, *MNRAS*, 483, 392
 Diaz, J. D., & Bekki, K. 2012, *ApJ*, 750, 36
 Dobbie, P. D., Cole, A. A., Subramaniam, A., & Keller, S. 2014, *MNRAS*, 442, 1663
 D’Onghia, E., & Fox, A. J. 2016, *ARA&A*, 54, 363
 Evans, C. J., & Howarth, I. D. 2008, *MNRAS*, 386, 826
 Fox, A. J., Richter, P., Wakker, B. P., et al. 2013, *ApJ*, 772, 110
 Gaia Collaboration, Helmi, A., van Leeuwen, F., et al. 2018, *A&A*, 616, A12
 Gardiner, L. T., & Noguchi, M. 1996, *MNRAS*, 278, 191
 Harris, J., & Zaritsky, D. 2006, *AJ*, 131, 2514
 Hindman, J. V. 1967, *AJPh*, 20, 147
 Hindman, J. V., Kerr, F. J., & McGee, R. X. 1963, *AJPh*, 16, 570
 HI4PI Collaboration, Ben Bekhti, N., Flöer, L., et al. 2016, *A&A*, 594, A116
 Hunter, J. D. 2007, *CSE*, 9, 90
 Jacyszyn-Dobrzyniecka, A. M., Skowron, D. M., Mróz, P., et al. 2016, *AcA*, 66, 149
 Jameson, K. E., Bolatto, A. D., Leroy, A. K., et al. 2016, *ApJ*, 825, 12
 Kallivayalil, N., van der Marel, R. P., Besla, G., Anderson, J., & Alcock, C. 2013, *ApJ*, 764, 161
 Kerr, F. J., Hindman, J. F., & Robinson, B. J. 1954, *AJPh*, 7, 297
 Lamb, J. B., Oey, M. S., Segura-Cox, D. M., et al. 2016, *ApJ*, 817, 113
 Leroy, A., Bolatto, A., Stanimirović, S., et al. 2007, *ApJ*, 658, 1027
 Massey, P. 2002, *ApJS*, 141, 81
 Mathewson, D. S., Cleary, M. N., & Murray, J. D. 1974, *ApJ*, 190, 291
 Mathewson, D. S., & Ford, V. L. 1984, in IAU Symp. 108, *Structure and Evolution of the Magellanic Clouds*, ed. S. van den Bergh & K. S. D. de Boer (Berlin: Springer), 125
 Mathewson, D. S., Ford, V. L., & Visvanathan, N. 1986, *ApJ*, 301, 664
 Mathewson, D. S., Ford, V. L., & Visvanathan, N. 1988, *ApJ*, 333, 617
 McClure-Griffiths, N. M., Dénes, H., Dickey, J. M., et al. 2018, *NatAs*, 2, 901
 Murai, T., & Fujimoto, M. 1980, *PASJ*, 32, 581
 Nidever, D. L., Monachesi, A., Bell, E. F., et al. 2013, *ApJ*, 779, 145
 Niederhofer, F., Cioni, M.-R. L., Rubele, S., et al. 2018, *A&A*, 613, L8
 Oey, M. S., Dorigo Jones, J., Castro, N., et al. 2018, *ApJL*, 867, L8
 Piatek, S., Pryor, C., & Olszewski, E. W. 2008, *AJ*, 135, 1024
 Putman, M. E., Gibson, B. K., Staveley-Smith, L., et al. 1998, *Natur*, 394, 752
 Rafelski, M., Gardner, J. P., Fumagalli, M., et al. 2016, *ApJ*, 825, 87
 Rippepi, V., Cioni, M.-R. L., Moretti, M. I., et al. 2017, *MNRAS*, 472, 808
 Russell, S. C., & Dopita, M. A. 1992, *ApJ*, 384, 508
 Scowcroft, V., Freedman, W. L., Madore, B. F., et al. 2016, *ApJ*, 816, 49
 Songaila, A., Blades, J. C., Hu, E. M., & Cowie, L. L. 1986, *ApJ*, 303, 198
 Stanimirović, S., Staveley-Smith, L., Dickey, J. M., Sault, R. J., & Snowden, S. L. 1999, *MNRAS*, 302, 417
 Stanimirović, S., Staveley-Smith, L., & Jones, P. A. 2004, *ApJ*, 604, 176
 Staveley-Smith, L., Sault, R. J., Hatzidimitriou, D., Kesteven, M. J., & McConnell, D. 1997, *MNRAS*, 289, 225
 Subramanian, S., & Subramaniam, A. 2012, *ApJ*, 744, 128
 Sylos Labini, F., Benhaïem, D., Comerón, S., & López-Corredoira, M. 2019, *A&A*, 622, A58
 van der Marel, R. P., Alves, D. R., Hardy, E., & Suntzeff, N. B. 2002, *AJ*, 124, 2639
 van der Marel, R. P., & Cioni, M.-R. L. 2001, *AJ*, 122, 1807
 van der Marel, R. P., & Sahlmann, J. 2016, *ApJL*, 832, L23
 Van Der Walt, S., Colbert, S. C., & Varoquaux, G. 2011, *CSE*, 13, 22
 Wayte, S. R. 1990, *ApJ*, 355, 473
 Welty, D. E., Xue, R., & Wong, T. 2012, *ApJ*, 745, 173
 Wolfe, A. M., & Chen, H.-W. 2006, *ApJ*, 652, 981
 Zivick, P., Kallivayalil, N., Besla, G., et al. 2019, *ApJ*, 874, 78
 Zivick, P., Kallivayalil, N., van der Marel, R. P., et al. 2018, *ApJ*, 864, 55